Correlated Anion-Disorder in Heteroanionic Cubic TiOF2

Christophe Legein, Benjamin J Morgan, Alexander G Squires, Monique Body, Wei Li, Mario Burbano, Mathieu Salanne, Thibault Charpentier, Olaf J Borkiewicz, Damien Dambournet

JACS
JOURNAL OF THE AMERICAN CHEMICAL SOCIETY
pubs.acs.org/JACS

Article

Correlated Anion Disorder in Heteroanionic Cubic $TiOF_2$

Christophe Legein,* Benjamin J. Morgan,* Alexander G. Squires, Monique Body, Wei Li, Mario Burbano, Mathieu Salanne, Thibault Charpentier, Olaf J. Borkiewicz, and Damien Dambournet*

Cite This: J. Am. Chem. Soc. 2024, 146, 21889−21902

Read Online

ACCESS | Metrics & More | Article Recommendations | Supporting Information

ABSTRACT: Resolving anion configurations in heteroanionic materials is crucial for understanding and controlling their properties. For anion-disordered oxyfluorides, conventional Bragg diffraction cannot fully resolve the anionic structure, necessitating alternative structure determination methods. We have investigated the anionic structure of anion-disordered cubic (ReO_3-type) $TiOF_2$ using X-ray pair distribution function (PDF), ^{19}F MAS NMR analysis, density functional theory (DFT), cluster expansion modeling, and genetic-algorithm structure prediction. Our computational data predict short-range anion ordering in $TiOF_2$, characterized by predominant *cis*-$[O_2F_4]$ titanium coordination, resulting in correlated anion disorder at longer ranges. To validate our predictions, we generated partially disordered supercells using genetic-algorithm structure prediction and computed simulated X-ray PDF data and ^{19}F MAS NMR spectra, which we compared directly to experimental data. To construct our simulated ^{19}F NMR spectra, we derived new transformation functions for mapping calculated magnetic shieldings to predicted magnetic chemical shifts in titanium (oxy)fluorides, obtained by fitting DFT-calculated magnetic shieldings to previously published experimental chemical shift data for TiF_4. We find good agreement between our simulated and experimental data, which supports our computationally predicted structural model and demonstrates the effectiveness of complementary experimental and computational techniques in resolving anionic structure in anion-disordered oxyfluorides. From additional DFT calculations, we predict that increasing anion disorder makes lithium intercalation more favorable by, on average, up to 2 eV, highlighting the significant effect of variations in short-range order on the intercalation properties of anion-disordered materials.

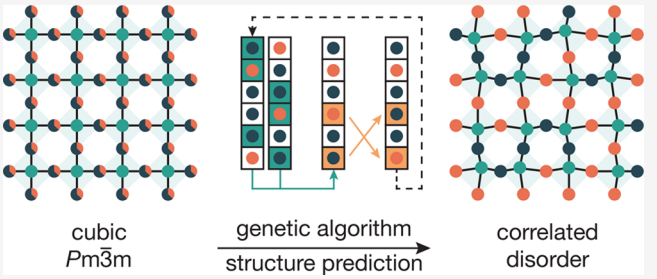

1. INTRODUCTION

Heteroanionic materials, which contain two or more anionic species, offer compositional and structural flexibility not found in otherwise analogous homoanionic materials.[1−4] As such, controlling the relative stoichiometries and crystallographic arrangements of the anion species in heteroanionic materials allows their properties to be tuned.[5,6] This compositional and structural versatility means that heteroanionic materials find applications across a range of critical technologies, including thermoelectrics,[7] photocatalysis,[8,9] and energy storage.[10−13]

The properties of heteroanionic materials depend on their chemical composition, specifically the identities and relative stoichiometries of their constituent anions, and on their structure, particularly the arrangement of these anions within their host crystal structure. While some heteroanionic materials are crystallographically ordered, with their constituent anion species arranged in a regular, repeating pattern, others are crystallographically disordered, with their anion species randomly distributed across crystallographically equivalent sites. In these anion-disordered systems, at long range, the site occupations of these anion species are uncorrelated. At short range, however, these different anion species often exhibit short-range ordering, characterized by one or more local configurations of anions appearing more frequently than in a fully uncorrelated (maximum entropy) anion distribution.

While experimental techniques that probe long-range correlations between atoms, such as X-ray or neutron Bragg scattering, can determine the average crystal structure of anion-disordered materials, these methods cannot resolve any short-range ordering, if present. Instead, these methods yield only an effective unit cell where each anion site is occupied by a statistical average of the constituent anion species. Short-range structural information can be obtained from scattering experiments in the form of pair distribution function (PDF) data.[14] However, for heteroanionic materials containing anions with similar X-ray or neutron scattering factors, such as oxyfluorides, it is often not possible to assign anion site occupations based solely on PDF data, and alternative methods must be used to resolve the anionic structure of these materials.

Received: May 13, 2024
Revised: July 6, 2024
Accepted: July 9, 2024
Published: July 26, 2024

One method that has proven effective for studying the short-range structure of heteroanionic materials is solid-state nuclear magnetic resonance (NMR) spectroscopy, which provides direct information about the local chemical environments of individual chemical species. In the case of oxyfluorides, the use of NMR spectroscopy is facilitated by the high gyromagnetic ratio and broad chemical shift range of the sole natural isotope of fluorine, ^{19}F, and several previous studies have used ^{19}F NMR spectroscopy to study oxygen−fluorine ordering in oxyfluorides.[15−27] However, using ^{19}F NMR data alone to unambiguously determine O/F ordering in disordered oxyfluorides can be challenging, due to the large number of possible anion permutations that might need to be considered; as a consequence, complementary experimental or computational data are often required to fully solve the anion structure.

Another approach to probing short-range order in heteroanionic materials is to use computational electronic structure methods, such as Density Functional Theory (DFT).[28,29] By calculating the relative energies of structures with varied anion configurations, low-energy anion structures can be identified directly. The high computational cost of electronic structure methods, however, limits their use to relatively small computational cells and to relatively small numbers of possible anion orderings, making it difficult to fully characterize the anion substructure in partially disordered materials. In these cases, it is necessary to use alternative computational methods that accurately describe correlations in anion site occupations at length scales beyond those typical of electronic structure calculations and ideally allow for rapid evaluation of possible anion arrangements.

Here, we report an investigation of the anionic structure in the anion-disordered transition-metal oxyfluoride, cubic (ReO_3-type) $TiOF_2$. Cubic $TiOF_2$ has previously been studied as a lithium-ion electrode material[30,31] and as a photocatalyst.[32,33] The average structure of cubic $TiOF_2$ consists of corner-sharing $Ti[O,F]_6$ octahedra within a cubic $Pm\bar{3}m$ space group (Figure 1). A previous X-ray diffraction study of cubic $TiOF_2$ found no evidence for anion ordering, and, on this basis, it was suggested that oxygen and fluorine are fully disordered (uncorrelated) over the available Wyckoff 3d sites.[34] Short-range ordering of oxygen and fluorine anions, however, is known in other ReO_3-type transition-metal oxyfluorides, such as NbO_2F and TaO_2F,[26,35−38] and it is therefore reasonable to ask whether ReO_3-type $TiOF_2$ might also exhibit short-range anion ordering.

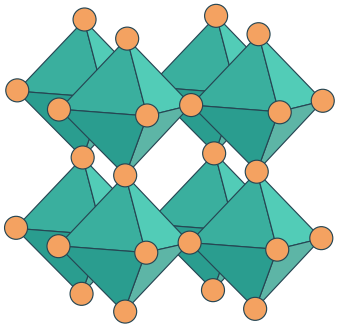

Figure 1. The cubic ReO_3-type structure (space group $Pm\bar{3}m$), comprised of corner-sharing MX_6 octahedra.

Using a combination of DFT calculations and cluster expansion modeling, we predict strong short-range ordering in ReO_3-type $TiOF_2$, characterized by an absence of collinear O−Ti−O units and a preference for polar *cis*-TiO_2F_4 titanium coordination. This polar coordination around titanium allows shorter Ti−O bonds and longer Ti−F bonds relative to the conventional $Pm\bar{3}m$ structure, which gives increased net bonding relative to *trans*-TiO_2F_4 titanium coordination. The preferential *cis*-TiO_2F_4 coordination also results in correlated anion disorder,[12,39,40] which gives uncorrelated anion site occupations at longer distances, in agreement with the average $Pm\bar{3}m$ structure assigned from long-length-scale diffraction data.[34]

To validate our computationally predicted structural model, we use a genetic algorithm (GA) to generate structures with partial thermal disorder, which we use as structural models for as-synthesized ReO_3-type $TiOF_2$. We then compute simulated PDF and ^{19}F NMR data for these GA-predicted structures and compare these to corresponding experimental PDF and ^{19}F NMR data. To generate our simulated ^{19}F NMR spectra, we convert from DFT-calculated magnetic shieldings to (calculated) chemical shifts using an empirical transformation function that we derive by fitting calculated magnetic shielding data for TiF_4 to previously reported experimental ^{19}F NMR data.[41] For both the PDF and ^{19}F NMR data, we observe good agreement between our simulated data for the GA-predicted structural model and our experimental data, supporting our computationally predicted structural model.

We also perform additional DFT calculations to evaluate how the degree of oxygen/fluorine ordering in ReO_3-type $TiOF_2$ affects its lithium intercalation properties. We find that increasing anion disorder makes lithium intercalation more favorable by, on average, up to 2 eV. This result suggests that the electrochemical properties of ReO_3-type $TiOF_2$, and potentially other heteroanionic intercalation electrode materials, can be controlled through synthesis protocols designed to produce samples with specific degrees of short-range anion order.

2. METHODS

2.1. Experimental Details. $TiOF_2$ was synthesized following the method described in ref 42. The synthesized compound was subsequently treated at 170 °C under vacuum to remove OH groups.

X-ray powder diffraction analysis was performed using a Rigaku Ultima IV X-ray diffractometer equipped with a Cu Kα radiation source (λ = 1.54059 Å). X-ray total scattering data were collected at the 11-ID-B beamline at the Advanced Photon Source, Argonne National Laboratory, using high-energy X-rays (λ = 0.2128 Å) up to a high momentum transfer value, Q_{max} = 18 Å^{-1}.[43,44] The raw total scattering data were processed using Fit2D.[45] Pair distribution function (PDF) data, $G(r)$, were derived by Fourier transformation after eliminating Kapton and background contributions using PDFGetX2.[46] Refinement of the PDF data was performed using PDFGui,[47] setting the Q_{damp} parameter at 0.04. The refined parameters included the lattice parameter, the scale factor, s_{ratio}—the correction for the low-r to high-r PDF peak ratio due to correlated motion of bonded atoms[48]—and isotropic atomic displacement factors.

^{19}F solid-state magic angle spinning (MAS) NMR experiments were performed on a Bruker Avance III spectrometer operating at 7.0 T (^{19}F Larmor frequency of 282.2 MHz), using a 1.3 mm CP-MAS probe head. Room-temperature ^{19}F MAS spectra were recorded using a Hahn echo sequence with an interpulse delay equal to one rotor period. The 90° pulse length was set to 1.55 μs, and the recycle delay was set to 20 s. ^{19}F spectra were referenced to $CFCl_3$ and fitted using the DMFit software.[49]

2.2. Computational Details. To model the relative energies of competing O/F anion configurations within the ReO_3-type $TiOF_2$

https://doi.org/10.1021/jacs.4c06304
J. Am. Chem. Soc. 2024, 146, 21889−21902

structure, we fitted a cluster expansion model to DFT-calculated energies of 65 symmetry-inequivalent 2×2×2 supercells. These 65 supercells were sampled from the complete set of 2664 symmetry-inequivalent 2×2×2 supercells of ReO_3-type $TiOF_2$, which we enumerated using BSYM.[50] These DFT calculations were performed using the VASP code,[51,52] with a plane-wave cutoff energy of 700 eV and a 4×4×4 Monkhorst−Pack *k*-point grid. The interactions between core and valence electrons were described using the projector augmented wave method,[53] with cores configurations of [Mg] for Ti, [He] for O, and [He] for F; for Li, all electrons were treated as valence. These calculations used the revised Perdew−Burke−Ernzerhof generalized gradient approximation (GGA) functional (PBEsol),[54] with a Dudarev +*U* correction applied to the Ti d states (GGA+*U*).[55,56] A value of $U_{Ti,d}$ = 4.2 eV was used, as for previous calculations on TiO_2,[57,58] Li-intercalated TiO_2,[59−61] and Ti-deficient hydroxyfluorinated anatase TiO_2.[62−64]

For our cluster expansion model training set, we performed full geometry optimizations, allowing changes to the cell shape and volume as well as internal atomic coordinates. Each geometry optimization was deemed converged when all atomic forces were smaller than 0.01 eV $Å^{-1}$. Our cluster expansion model was fitted using the MAPS component of the ATAT code,[65,66] which produced a model with 10 nonzero ECIs and a cross-validation score of 0.013 eV per structure.[67] Additional information about the cluster expansion fitting and resulting model are provided in the Supporting Information (SI).

To quantify bond strengths for the structures in our training set of 65 2×2×2 supercells, we calculated Ti−(O/F) integrated crystal-orbital Hamilton populations (iCOHPs) using the LOBSTER code,[68−70] with VASPFITPBE2015 basis functions used to map the VASP plane-wave basis set onto local orbitals.

To validate our structural model, we generated larger $TiOF_2$ structures (4×4×4 supercells) using a genetic algorithm (GA) for structure prediction. Our GA used a combination of elitist and proportionate selection, with selection probabilities based on a Boltzmann fitness function and energies of competing configurations calculated using our DFT-derived cluster expansion model. Full details of this GA are provided in the SI.

Using our GA structure prediction protocol, we generated four $TiOF_2$ 4×4×4 supercells for validation against our experimental PDF and ^{19}F NMR data. For each supercell, we initially relaxed atomic positions and cell volume (fixed cell shape) in VASP, using the parameters described above and a 2×2×2 Monkhorst−Pack *k*-point grid. For input structures for ^{19}F NMR spectra calculations, we then performed a full optimization (atomic positions, cell volume, and cell shape) using CP2K,[71] using the PBE GGA exchange-correlation functional[72] and the DFT-D3 dispersion-correction method of Grimme et al.,[73] which corrects for the overestimation of bond-lengths and cell volumes found for typical PBE calculations.[74] The CP2K calculations used Goedecker−Teter−Hutter (GTH) pseudopotentials[75] and TZVP Gaussian basis sets (MOLOPT library), with a charge density plane-wave expansion energy cutoff of 720 Ry.

The ^{19}F magnetic-shielding tensors for these geometry-optimized $TiOF_2$ 4×4×4 supercells were calculated using the GIPAW approach[76,77] within VASP,[51,78] using the PBE GGA exchange-correlation functional[72] with a 550 eV plane-wave cutoff and a 2×2×2 Monkhorst−Pack *k*-point grid. The simulated ^{19}F MAS NMR spectra were constructed from the DFT-calculated ^{19}F magnetic shielding data using the procedure described in ref 79. For each fluorine atom, a MAS NMR spectrum was simulated, given the relevant experimental values of spin rate (64 kHz) and the magnetic field (7 T). The full MAS NMR spectrum for a given structural model was then obtained by summing the spectra for all the constituent fluorine atoms. The simulated ^{19}F NMR spectra were computed using the FPNMR package.[79]

To generate simulated ^{19}F NMR spectra from DFT calculations, it is necessary to convert calculated isotropic magnetic shieldings, σ_{iso}, and magnetic shielding anisotropies, σ_{csa}, to isotropic chemical shifts, δ_{iso}, and chemical shift anisotropies, δ_{csa}, respectively.[80] Suitable transformation functions were obtained by fitting linear models for $\sigma_{iso}\rightarrow\delta_{iso}$ and for $\sigma_{csa}\rightarrow\delta_{csa}$ using linear least-squares regression between calculated magnetic shielding data for TiF_4 and corresponding chemical shift data previously reported.[41] A full discussion of the derivation of these transformation functions is given in Section 3.4.4.

The calculation of the ^{19}F magnetic shielding tensors for TiF_4 was performed using the GIPAW approach[76,77] within VASP.[51,78] The TiF_4 input structure for these reference magnetic shielding calculations was obtained from a geometry optimization performed in VASP,[51,78] where only atomic coordinates were relaxed, keeping the cell parameters fixed to experimental values. This geometry optimization used Ti [Ne] and F [He] pseudopotentials and the Perdew−Burke−Ernzerhof (PBE) GGA functional, augmented with the DFT-D3 correction of Grimme et al.,[73] to account for dispersion interactions between the isolated columns of corner-linked TiF_6 octahedra that comprise the TiF_4 structure.[41,81] Both the geometry optimization calculation and the subsequent ^{19}F NMR calculation used a plane-wave cutoff of 550 eV and a 1×6×3 Monkhorst−Pack *k*-point grid.

Additional results from calculations of the ^{19}F magnetic shielding tensors for TiF_4, performed with optimization of atomic positions but without the DFT-D3 correction, using CASTEP[82,83] (to replicate the previous calculations of Murakami et al.[41]) and VASP, are provided in the SI. The SI includes additional details on the effects that different optimization and relaxation protocols have on the resulting TiF_4 structure.

Lithium intercalation calculations were performed for three exemplar 4×4×4 $TiOF_2$ supercells: one genetic-algorithm (GA)-predicted structure, a 4×4×4 supercell special quasi-random structure, and a 4×4×4 expansion of the DFT-predicted lowest-energy 2×2×2 structure. For each structure, we considered lithium intercalation at all nonequivalent cubic interstitial sites and performed geometry relaxations with lattice parameters fixed to those of the corresponding stoichiometric $TiOF_2$ model. These calculations used a cutoff energy of 500 eV and a 2×2×2 Monkhorst−Pack *k*-point grid. To calculate lithium intercalation energies, elemental (metallic) lithium was modeled using a Li_2 cell, with a cutoff energy of 500 eV and a 16×16×16 Monkhorst−Pack *k*-point grid.

3. RESULTS AND DISCUSSION

3.1. X-ray Diffraction and PDF Analysis. Our X-ray diffraction data index to a $Pm\bar{3}m$ structure (SI Figure S1) with a cell parameter of a_0 = (3.8076 ± 0.0001) Å, consistent with the value of a_0 = (3.798 ± 0.005) Å reported by Vorres and Donohue.[34] This result corresponds to a ReO_3-type structural model, comprised of symmetric corner-sharing TiX_6 octahedra with a single Ti−X nearest-neighbor distance of 1.899 Å.

Given the different formal charges of O^{2-} and F^-, these anions are expected to exhibit differentiated bonding with Ti, resulting in distinct Ti−O and Ti−F bond lengths. In an anion-ordered system, differences in Ti−O and Ti−F bond lengths should theoretically be observable in the long-range diffraction data as a reduction in crystal symmetry from $Pm\bar{3}m$. However, the absence of any observable deviation from $Pm\bar{3}m$ symmetry in our X-ray diffraction data indicates that, at long ranges, the positions of oxygen and fluorine are uncorrelated, giving an average high-symmetry $Pm\bar{3}m$ structure. This observation aligns with the previous study by Vorres and Donohue,[34] wherein the absence of long-range O/F correlations in ReO_3-type $TiOF_2$ was interpreted as evidence that O and F are randomly distributed across the available Wyckoff 3d positions.

To better understand the anionic substructure of ReO_3-type $TiOF_2$, we consider the pair distribution function obtained from X-ray total scattering data. For interatomic distances between 8 and 40 Å, the PDF data are well described by a cubic $Pm\bar{3}m$ model (R_w = 13.2% (SI Figure S2), in agreement

https://doi.org/10.1021/jacs.4c06304
J. Am. Chem. Soc. 2024, 146, 21889−21902

with the X-ray diffraction analysis above. The experimental PDF for $r < 8$ Å, however, gives a poor fit ($R_w = 31.2\%$) when modeled with a cubic ReO_3-type ($Pm\bar{3}m$) structure (Figure 2),

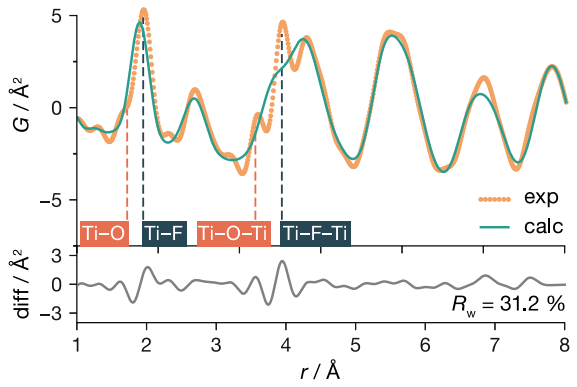

Figure 2. PDF refinement of cubic $TiOF_2$ using the cubic ReO_3-type ($Pm\bar{3}m$) structure model.

indicating deviations from the average ReO_3-type structure at short range. Notably, we observe apparent splittings in the nearest-neighbor Ti–X peak at ~1.9 Å and in the next-nearest-neighbor peak at ~3.8 Å, suggesting distinct bonding environments. Based on the expectation that Ti–O bonding will, in general, be stronger than Ti–F bonding,[35] we preliminarily assign the peaks at 1.71 and 1.94 Å to Ti–O and Ti–F nearest-neighbor pairs, respectively, and the peaks at 3.55 and 3.93 Å to Ti–(O)–Ti and Ti–(F)–Ti next-nearest-neighbor cation pairs, respectively.

3.2. ^{19}F NMR. Figure 3 shows the ^{19}F MAS solid-state NMR spectrum for ReO_3-type $TiOF_2$, which provides

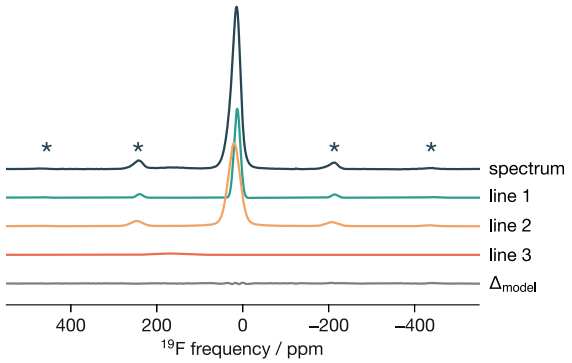

Figure 3. Experimental and fitted ^{19}F MAS (64 kHz) NMR spectra of ReO_3-type $TiOF_2$. The individual resonances obtained from the fit are presented in Table I. Spinning sidebands of the main contribution are indicated by asterisks.

additional information about the local environments of the F^- anions. The spectrum shows a broad, slightly asymmetric main feature. We have reconstructed the experimental spectrum using two resonances (lines 1 and 2), which we assign to bridging Ti–F–Ti fluorine atoms. Additionally, our reconstruction reveals a broader and less intense line (line 3) at $\delta_{iso} \approx 170$ ppm, which we attribute to Ti–F–□ "non-bridging" fluorine atoms, where one adjacent titanium site is vacant.[42,84]

The asymmetry and width of the main peak in the ^{19}F NMR spectrum suggest that our ReO_3-type $TiOF_2$ sample contains multiple distinct fluoride-ion environments. Previous studies have reported that $TiOF_2$ prepared by aqueous solution synthesis contains hydroxyl defects and metal vacancies.[42] The relative intensities of the fitted ^{19}F NMR resonances (Table I)

Table I. δ_{iso} (ppm), δ_{csa} (ppm), η_{csa}, Line Widths (ppm), and Relative Intensities[a]

	δ_{iso}	δ_{csa}	η_{csa}	LW	I	assignment
line 1	12.8	−159	0.65	17.1	32.0	Ti–F–Ti
line 2	20.0	−204	0.00	31.8	65.8	Ti–F–Ti
line 3	169.2	−113	0.00	80.6	2.2	Ti–F–□

[a]Averaging over lines 1 and 2 gives a weighted average for bridging Ti–F–Ti environments $\langle\delta_{iso}\rangle = 17.6$ ppm.

indicate that only 2.2% of F^- ions are "non-bridging" in our sample, implying a relatively high stoichiometric purity, with a Ti vacancy concentration of $\lesssim$0.5%.[85] This low Ti-vacancy concentration is insufficient to explain the asymmetry and breadth of the main peak in the ^{19}F NMR data. Instead, we interpret these features as indicative of O/F disorder, which is expected to produce a range of local fluoride-ion environments and a corresponding distribution of Ti–F bond lengths.

3.3. DFT + Cluster Expansion Modeling. To further explore the nature of O/F disorder in ReO_3-type $TiOF_2$, we conducted a computational analysis of all possible 2×2×2 $TiOF_2$ supercells ($Ti_8O_8F_{16}$), consisting of 2664 distinct symmetry-inequivalent O/F configurations. To efficiently compute the relative energies of all 2664 structures, we first performed DFT calculations on a subset of 65 structures and used these results to fit a cluster-expansion model, as described in the Methods section. This cluster-expansion model was then used to calculate the energies of all 2664 2×2×2 supercells. The resulting configurational density of states for all 2×2×2 $TiOF_2$ supercells (Figure 4a) reveals an energy difference of 0.94 eV per formula unit between the configurations with the lowest and highest energies. This energy variation between different anion configurations indicates a strong energetic preference for certain short-range anion configurations over others, consistent with short-range ordering. This finding contradicts the previously proposed structural model that O and F positions in ReO_3-type $TiOF_2$ are completely uncorrelated,[34] which instead implies equal energies for all 2×2×2 $TiOF_2$ cells.

ReO_3-type $TiOF_2$ is chemically and structurally similar to ReO_3-type NbO_2F and TaO_2F. In these materials, it has been proposed that collinear F–M–F units are disfavored and that oxygen and fluorine anions preferentially adopt short-range orderings that give asymmetric F–M–O units.[35] This coordination asymmetry allows the central cation to shift off-center to form shorter Ti–O bonds, which has been suggested to increase the overall bonding strength of the $M(O/F)_6$ unit. By analogy, we might anticipate that, in $TiOF_2$, collinear O–Ti–O units are disfavored compared to asymmetric collinear O–Ti–F units. Figure 4b shows the distribution of energies for all 2×2×2 supercells, grouped by the number of collinear O–Ti–O units in each structure, out of a maximum of 8 possible for this supercell size. In general, structures with a greater number of collinear O–Ti–O units have higher configurational energies, while the lowest energy structures have no collinear O–Ti–O subunits. This observed correlation supports the hypothesis that, in ReO_3-type $TiOF_2$, oxygen and fluorine preferentially organize to give asymmetric collinear O–Ti–F units.

https://doi.org/10.1021/jacs.4c06304
J. Am. Chem. Soc. 2024, 146, 21889–21902

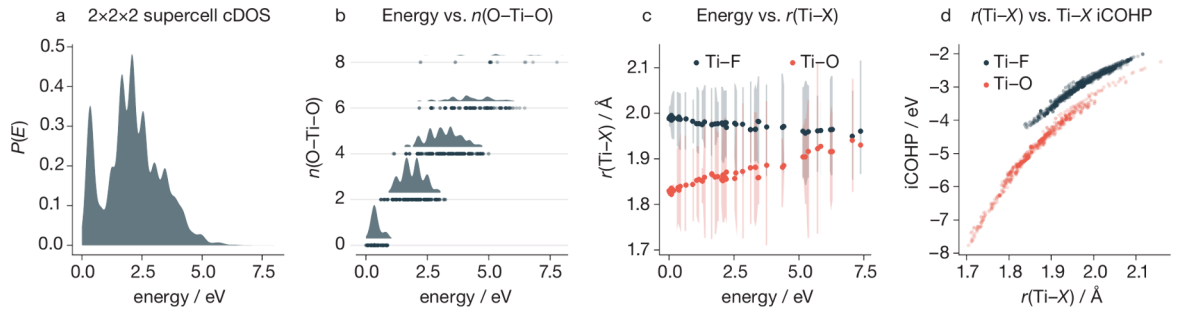

Figure 4. (a) Configurational density of states (cDOS) for a 2×2×2 supercell of $TiOF_2$, calculated from our cluster expansion model. (b) Energies of 2×2×2 supercells of $TiOF_2$, categorized by the number of collinear O−Ti−O units, and the corresponding cDOS contributions. (c) Ti−(O/F) bond lengths as a function of relative energy per structure for the set of 65 DFT-optimized 2×2×2 $TiOF_2$ supercells. Solid circles show average Ti−O and Ti−F distances for each configuration. Vertical shading shows the 5th−95th percentile range for Ti−O and Ti−F distances, for all structures within a 0.1 eV moving window. (d) Bond length versus bond iCOHP for all Ti−O and Ti−F nearest neighbors in the set of DFT calculations. More negative iCOHP values correspond to stronger bonding.

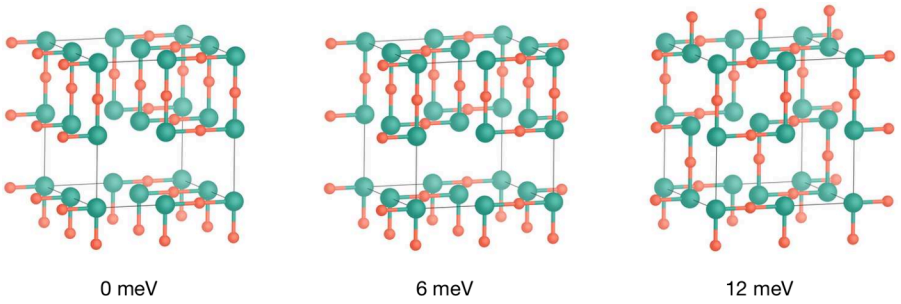

Figure 5. The three lowest-energy 2×2×2 supercells of $TiOF_2$ predicted by the DFT-parametrized cluster expansion model and their relative energies per $TiOF_2$ formula unit.

Figure 5 displays the three lowest energy 2×2×2 $TiOF_2$ structures, all of which are comprised entirely of *cis*-Ti-$[O_2F_4]$ subunits. This local coordination achieves local electroneutrality, in accordance with Pauling's second rule,[86] while also avoiding collinear O−Ti−O subunits. The energy difference between these three low-energy structures is only 12 meV, and all 2×2×2 structures containing only *cis*-Ti-$[O_2F_4]$ units are within 80 meV of the lowest energy structure. Consequently, our calculations predict that ReO_3-type $TiOF_2$ exhibits a preference for polar *cis*-Ti-$[O_2F_4]$ coordination, but these *cis*-Ti-$[O_2F_4]$ units are expected to adopt a variety of different relative arrangements within the crystal structure, resulting in correlated anion disorder.[12,39,40]

The preference for polar *cis*-Ti-$[O_2F_4]$ over nonpolar *trans*-Ti$[O_2F_4]$ coordination in ReO_3-type $TiOF_2$, as predicted here, echoes the preference for polar cation coordination reported in other transition-metal oxyfluorides and oxynitrides.[1,29,35,87−95] In these materials, the preference for *cis*- versus *trans*-MX_2Y_4 or *fac*- versus *mer*-MX_3Y_3 coordination has been attributed to the property of a polar configuration of anions: the central cation can move off-center, resulting in shorter M−O distances and stronger net cation−anion bonding. Our results for ReO_3-type $TiOF_2$ are consistent with this model—the lowest energy structures from our calculations, which are composed entirely of *cis*-Ti-$[O_2F_4]$ units, have short Ti−O bonds (∼1.82 Å) and longer Ti−F bonds (∼1.99 Å), in agreement with our assignment of the split first peak in our experimental short-range PDF data (Figure 2). Further evidence for lower energy anion configurations being those that allow shorter Ti−O bonds and longer Ti−F bonds is provided by Figure 4c, which plots the Ti−O and Ti−F bond lengths for all 65 DFT-optimized 2×2×2 supercells in the cluster-expansion model training set as a function of energy relative to the lowest energy structure. In general, lower energy structures have shorter mean Ti−O bonds and slightly longer mean Ti−F bonds, whereas in the highest energy structures the mean Ti−O and mean Ti−F bond lengths are nearly identical (Figure 4c).

To further quantify the relationship between the Ti−(O/F) bond lengths and bonding strength, we calculated integrated iCOHPs for each Ti−(O/F) bond in our DFT data set, which are plotted against the corresponding bond lengths in Figure 4d. iCOHP values serve as indicators of bonding strength, with more negative values attributed to stronger and more covalent bonding.[68−70] Both Ti−O and Ti−F bonds are predicted to become stronger as the Ti−(O/F) distance decreases. Moreover, both plots of bond strength versus bond length are concave, which indicates that Ti centers with a mix of shorter-than-average and longer-than-average bonds Ti−X bonds have greater net bond strength than Ti centers where all six Ti−X bonds are of equal length.

3.4. Genetic-Algorithm Structure Prediction, Intermediate-Range Ordering, and Validation against Experimental Data. *3.4.1. Genetic-Algorithm Structure Prediction.* The DFT and cluster-expansion analysis detailed above (Section 3.3) predicts that ReO_3-type $TiOF_2$ exhibits short-range anion order characterized by preferential *cis*-Ti$[O_2F_4]$ coordination. Our calculations also provide an explanation for this preference: anion configurations that avoid collinear O−Ti−O units allow local distortions from TiX_6 coordination with six equal-length Ti−X bonds, resulting in shorter Ti−O (and consequently longer Ti−F) bonds, thereby increasing the net Ti−X bonding.

https://doi.org/10.1021/jacs.4c06304
J. Am. Chem. Soc. 2024, 146, 21889−21902

The energetic preference for *cis*-Ti[O_2F_4] short-range ordering implies a ground-state structure with 100% *cis*-Ti[O_2F_4] coordination, which is consistent with the lowest energy 2×2×2 structures shown in Figure 5, each of which exhibits 100% ordered *cis*-Ti[O_2F_4] units. The calculated configurational density of states (cDOS) (Figure 4a), however, does not show a clear energy gap above the lowest energy 2×2×2 structure, and we instead predict multiple low-energy structures that may be expected to be competitive under synthesis.[12] Consequently, as-synthesized samples of ReO_3-type $TiOF_2$ are expected to exhibit some degree of partial disorder, while still demonstrating a general preference for local *cis*-Ti[O_2F_4] coordination.

To create structural models that incorporate this partial disorder, we used a genetic algorithm (GA) structure prediction scheme to generate a set of exemplar 4×4×4 supercells. For each structure prediction calculation, we initialized the GA with a starting population of 40 4×4×4 $TiOF_2$ supercells, each with random O and F anion configurations. The GA used a combination of elitist selection and proportional selection, employing a Boltzmann-weighted fitness function, $f_i \propto \exp(E_i/kT)$, to select structures from each generation for seeding the next generation (full details of the GA algorithm are given in the SI). The energies for each structure considered by the algorithm were calculated using our DFT-derived cluster expansion model. This GA structure prediction scheme is conceptually similar to running multiple concurrent Monte Carlo-based simulated annealing simulations, where structural motifs associated with low-energy configurations at any point can be shared across simulations. The GA algorithm quickly filters out high-energy, less probable structures to produce a pool of structures with energetically reasonable O/F anion configurations (Figure 6).

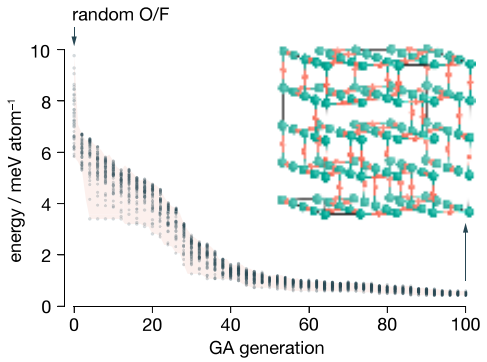

Figure 6. Evolution of energies of a population of 40 structures over 100 generations of the genetic algorithm structure prediction procedure. Generation 0 is initialized with a population of structures with random O/F configurations. Each shaded point shows the energy of a single structure within each generation. The inset shows one example supercell obtained as the lowest-energy structure after 100 GA generations.

Using this GA procedure, we generated four 4×4×4 supercells, with each selected as the lowest energy structure after 100 GA generations. The resulting 4×4×4 structures feature no collinear O−Ti−O units and predominantly exhibit *cis*-TiO_2F_4 coordination (93.0%), with some *fac*-TiO_3F_3 (3.5%) and $TiOF_5$ (3.5%) coordination (SI Figure S6). Additional analysis of the TiX_6 coordination geometries in these 4×4×4 models (see the SI) shows that the anions show small average deviations from ideal octahedra, while the mean Ti−O and Ti−F distances are significantly different, due to large off-center displacements of the Ti cations (averaging 0.20 Å).

3.4.2. Intermediate-Range Anion Ordering. Like cubic $TiOF_2$, NbO_2F also adopts an average ReO_3-type structure[26,96] with oxygen and fluorine distributed over the Wyckoff 3d positions. NbO_2F is believed to exhibit short-range ordering somewhat analogous to that predicted here for $TiOF_2$, with collinear F−Ti−F units disfavored.[35,36] Electron diffraction data for NbO_2F, however, show ⟨*hk*1/3⟩* sheets of diffuse intensity, which has been attributed to anion ordering in one-dimensional strings along each of the three ⟨001⟩ directions.[36] To explain this experimental observation, Brink et al. proposed a structural model for NbO_2F in which oxygen and fluorine are ordered along ⟨001⟩ strings in repeating [F−O−O−F] sequences but are uncorrelated between pairs of ⟨001⟩ strings, regardless of whether these strings are aligned along the same or different ⟨001⟩ directions.[36]

Motivated by this evidence for [F−O−O−F] anion ordering along ⟨100⟩ strings in ReO_3-structured NbO_2F,[97] we next considered whether ReO_3-type $TiOF_2$ can be predicted to exhibit analogous [O−F−F−O] ordering. To explore this possibility, we performed two sets of calculations. First, we used our GA structure prediction scheme with our DFT-derived cluster expansion model to generate a 6×6×6 supercell, with this supercell size chosen to accommodate anion orderings with a ×3 unit cell repeat distance. We then analyzed the resulting structure to determine the relative prevalence of different ⟨100⟩ orderings. Second, we computed DFT geometry-optimized energies for three sets of $TiOF_2$ structures with different supercell sizes (2×2×2, 3×3×3, and 4×4×4) and different ⟨100⟩ anion orderings to determine whether any of these ⟨100⟩ anion orderings is sufficiently energetically favored to predict general anion ordering.

The first calculation, using our GA structure prediction scheme, yielded a 6×6×6 supercell with the same local coordination preferences as for the GA-predicted 4×4×4 supercells. The resulting structure contains no collinear O−Ti−O units, and the TiX_6 coordination octahedra are predominantly *cis*-TiO_2F_4 (89.8%), with small proportions of *fac*-TiO_3F_3 (5.1%) and $TiOF_5$ (5.1%). This distribution of TiO_xF_{6-x} coordination octahedra differs significantly from that predicted by mapping the Brink et al.[36] NbO_2F model to $TiOF_2$, with *cis*-TiO_2F_4 (44.4%), *fac*-TiO_3F_3 (29.6%), $TiOF_5$ (22.2%), and TiF_6 (3.7%) (SI Figure S8).

Furthermore, in our 6×6×6 GA-predicted model, only 25 out of 108 ⟨001⟩ columns (23.1%) exhibit [O−F−F−O] ordering, while the Brink et al.[36] NbO_2F-type model predicts that all ⟨001⟩ columns should exhibit this ordering. While our 6×6×6 GA-predicted structure disagrees with both the distribution of cation coordination environments and the distribution of anion orderings along ⟨100⟩ columns predicted by the NbO_2F-type model, we do observe partial intermediate-range ordering. The proportion of columns with [O−F−F−O] anion sequences (23.1%) is higher than that expected for an equivalent supercell with a fully random arrangement of anions (6.6%). We attribute this effect to a second-order consequence of the short-range ordering in $TiOF_2$, where collinear O−Ti−O units are strongly disfavored, resulting in (partial) anion correlations at intermediate length scales.

Although our GA-predicted 6×6×6 supercell suggests that $TiOF_2$ does not exhibit NbO_2F-type exclusive [O−F−F−O]

https://doi.org/10.1021/jacs.4c06304
J. Am. Chem. Soc. 2024, 146, 21889−21902

ordering along ⟨100⟩ columns, this result might be a consequence of our choice of fitting procedure for the DFT-derived cluster expansion model used in the GA structure prediction scheme. Because our DFT training set includes only 2×2×2 supercells, only anion−anion interactions that fit within this supercell size are included in the resulting cluster expansion model.

To validate the predictions from our 6×6×6 GA structure prediction, we performed additional DFT calculations on a set of [O−F−F−O]-ordered 3×3×3 $TiOF_2$ supercells and compared the resulting energies (per formula unit) to those of the 2×2×2 supercells in our CE training set with exclusive *cis*-TiO_2F_4 cation coordination and to the DFT-optimized energies of our four 4×4×4 GA-predicted supercells. All three sets of structures have no collinear O−Ti−O units and, therefore, are expected to all have relatively low energies, but they have different anion ⟨100⟩ orderings: The 2×2×2 all-*cis*-$TiOF_2$ structures have exclusive [(F)−O−F−(O)] ⟨100⟩ ordering, the 3×3×3 structures have, by construction, exclusive [O−F−F−O] ordering, and the 4×4×4 GA-predicted supercells have a mixture of [O−F−F−F−O] and [O−F−O−F−O] ⟨100⟩ orderings.

By comparing the relative energies from all three sets of structures, we can directly test the hypothesis of favored Brink-type [O−F−F−O] anion-ordering in ReO_3-type $TiOF_2$. Under this hypothesis, we would expect the 3×3×3 [O−F−F−O] structures to have significantly lower energies than any of the 2×2×2 and 4×4×4 structures, which would predict that [O−F−F−O] ⟨100⟩ ordering forms preferentially during synthesis.

Figure 7 shows our DFT-calculated energies per $TiOF_2$ formula unit for each set of structures. While the lowest energy

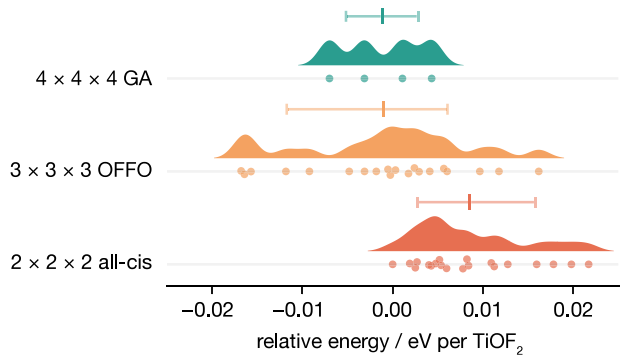

Figure 7. Raincloud plot[98] showing DFT-calculated relative energies per formula unit of (top) the 4×4×4 GA-predicted structures; (middle) 20 randomly generated 3×3×3 structures with 100% [O−F−F−O] ordering along the ⟨100⟩ columns; (bottom) the 100% *cis*-TiO_2F_4 2×2×2 supercells from the CE model DFT training set. Energies are given relative to the energy per formula unit of the lowest-energy 2×2×2 supercell. Error bars show the 16th−84th percentile range and mean relative energy per TiO_2F_4 unit for each data set.

structures of those computed are 3×3×3 [O−F−F−O]-ordered structures, these are not significantly more stable than the 2×2×2 and 4×4×4 structures, which both have no [O−F−F−O] ordering. All computed structures are within 0.04 eV per formula unit of the lowest energy structure. Moreover, we find some 3×3×3 [O−F−F−O]-ordered structures with slightly higher energies per formula unit than some 2×2×2 and all 4×4×4 structures.

These DFT results are consistent with the predictions from our 6×6×6 GA structure prediction: we find no evidence for preferential [O−F−F−O] ordering along ⟨100⟩ columns in ReO_3-type $TiOF_2$. [O−F−F−O] ordering does yield low-energy structures by avoiding disfavored collinear O−Ti−O units, but it is predicted to be present within a mixture of ⟨100⟩ orderings, such as [O−F−O] and [O−F−F−F−O], that also satisfy this condition.

3.4.3. GA Structure Validation versus PDF Data. To validate our computationally derived structural models for ReO_3-type $TiOF_2$, each GA-predicted 4×4×4 supercell was fully geometry-optimized using DFT and then used as input for direct comparison to our experimental PDF and NMR data.

To validate against the experimental PDF data, each GA-predicted structure was used as an initial structural model that was fitted to the experimental PDF data, with the atomic positions left unrefined to limit the number of fitting parameters. All four GA-predicted structures give a better fit for the experimental data than the average cubic $Pm\bar{3}m$ model (R_w = 31.2%), with the best fit obtained for GA structure 4 (R_w = 16.4%) (Figure 8). The improved fit to the experimental

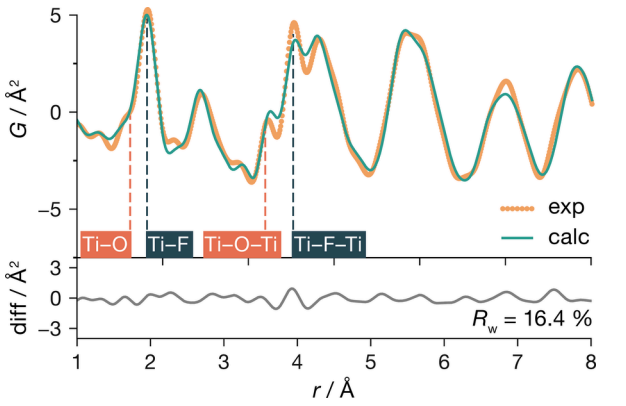

Figure 8. Comparison of the experimental PDF for cubic $TiOF_2$ with a simulated PDF from a 4×4×4 supercell generated by our genetic-algorithm structure prediction (GA structure 4).

PDF data is particularly evident in the split peak at 1.82 and 1.99 Å, which we previously assigned to nearest-neighbor Ti−O and Ti−F distances, respectively, and in the region between 3.5 and 4.0 Å, which we assigned to Ti−X−Ti pairs, and which is consistent with the observation from our 2×2×2 supercell DFT data set that ReO_3-type $TiOF_2$ preferentially adopts anion configurations that allow the Ti−O and Ti−F bond lengths to be shorter and longer, respectively, than the average Ti−X bond length of 1.90 Å. Our assignment of these peaks in the experimental PDF spectrum is also validated by direct analysis of the GA-predicted structures (SI), which gives mean Ti−O and Ti−F distances of 1.81 and 1.99 Å, respectively, and a clear splitting in Ti−X−Ti distances.

3.4.4. GA Structure Validation versus ^{19}F NMR MAS Data. To validate our GA-predicted structures against our experimental ^{19}F NMR MAS data, we performed DFT calculations on each of the four GA-predicted structures to calculate magnetic shielding tensors for each fluoride anion. Obtaining a simulated ^{19}F NMR spectrum from DFT calculations requires converting from calculated isotropic and anisotropic shielding values, σ_{iso} and σ_{csa}, to predicted isotropic and anisotropic chemical shift values, δ_{iso} and δ_{csa}, respectively.

https://doi.org/10.1021/jacs.4c06304
J. Am. Chem. Soc. 2024, 146, 21889−21902

For the isotropic values, the conventional approach to convert from σ_{iso} to δ_{iso} is to use a linear transformation function $\delta_{iso} = a\sigma_{iso} + b$, where the parameters a and b are obtained by linear regression between computed σ_{iso} and experimental δ_{iso} data. Several different linear transformation functions for ^{19}F have been published for a wide range of cations bonded to fluorine (see SI Table S4). One approach for the quantitative prediction of ^{19}F δ_{iso} values for a disordered system containing one metal cation is to derive an appropriate linear transformation function from data for a reference ordered (oxy)fluoride containing the same cation as the system of interest and with fluoride ions occupying multiple crystallographic sites. This approach has previously been used to simulate the ^{19}F NMR spectra of the disordered oxyfluorides MO_2F[26] and MOF_3[95] (M = Nb, Ta), with transformation functions derived by fitting to data for the corresponding MF_5 fluorides.[74]

For obtaining a transformation function $\sigma_{iso}\rightarrow\delta_{iso}$ for titanium (oxy)fluorides, a reasonable reference system is TiF_4. TiF_4 is formed from corner-sharing TiF_6 octahedra (Figure 9) and contains 12 inequivalent fluorine sites that can

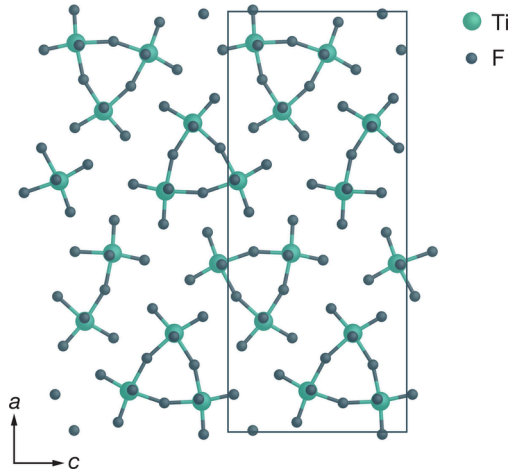

Figure 9. Structure of TiF_4,[41,81] showing the characteristic $[Ti_3F_{15}]$ rings which are connected along the b axis, and containing distinct bridging Ti−F−Ti and terminal Ti−F fluorine environments. Adapted with permission from ref 41. Copyright 2019 Elsevier.

be classified into two groups: bridging fluorine atoms, which are bonded to two titanium centers, and terminal fluorine atoms, which are bonded to only one titanium center.[41,81] High-resolution ^{19}F NMR data for TiF_4 have previously been reported by Murakami et al.,[41] who derived a linear $\sigma_{iso}\rightarrow\delta_{iso}$ transformation function by fitting this model function to DFT-calculated σ_{iso} and experimental δ_{iso} data.[99] While the DFT and experimental σ_{iso} and δ_{iso} data of Murakami et al. follow an approximately linear relationship, close inspection of these data (reproduced in SI Figure S10) shows that a single linear relationship is not able to accurately describe the correlations between σ_{iso} and δ_{iso} simultaneously for both bridging and terminal fluorine atoms, with each subset of atoms showing systematic deviations from the linear model obtained from fitting to all the fluorine atoms. Murakami et al. were also unable to obtain a satisfactory quantitative relationship between their calculated and experimental data for the magnetic anisotropies, which prevents the quantitative prediction of spinning side bands.

To address these limitations, and to derive transformation functions suitable for the simulation of ^{19}F NMR spectra of titanium (oxy)fluorides, we have revisited the analysis by Murakami et al.[41] Figure 10b shows calculated σ_{iso} data for TiF_4 plotted against the corresponding experimental δ_{iso} values reported by Murakami et al.[41] The data form two distinct clusters, corresponding to terminal and bridging F, at low and high σ_{iso} values, respectively. As reported by Murakami et al., the full data set does show an approximately linear relationship between σ_{iso} and δ_{iso} values. Zooming-in on the data for terminal and bridging fluorine atoms (Figure 10a and c, respectively), however, highlights the deficiencies of fitting a single linear model to both groups of data. The observation that these ^{19}F NMR data are not well described by a single linear relationship is, perhaps, unsurprising, given the significant difference in local chemical environment and bonding for fluorine atoms directly bonded to two versus one Ti centers. To account for the categorical difference between bridging and nonbridging fluorine atoms, we fit separate linear models to the two clusters of data. This approach is much better able to quantitatively describe the correlation between σ_{iso} and δ_{iso} within each category of fluorine atoms (bridging versus nonbridging), and we obtain best-fit linear relationships of $\delta_{iso} = -0.830\sigma_{iso} + 44.1$ for bridging F and $\delta_{iso} = -1.116\sigma_{iso} + 67.2$ for terminal F.

Figure 10d−f shows an equivalent treatment of the DFT-calculated σ_{csa} and experimentally derived δ_{csa} data. Fitting the linear relationship $\delta_{csa} = a\sigma_{csa}$ to the full σ_{csa} versus δ_{csa} data set (Figure 10e) gives a poor fit, with the data for terminal and bridging fluorine atoms showing systematic deviations from the average best-fit model. By fitting separate functions to the data for the terminal (Figure 10d) fluorine atoms and for the bridging (Figure 10f) fluorine atoms, respectively, however, we obtain two transformation functions that much more accurately describe the quantitative relationship between σ_{csa} and δ_{csa} in TiF_4.

In our GA-predicted models, all F's bridge between two Ti's. To generate simulated ^{19}F NMR spectra for these GA-predicted $TiOF_2$ structural models, we use the $\sigma_{iso}\rightarrow\delta_{iso}$ and $\sigma_{csa}\rightarrow\delta_{csa}$ relationships derived for bridging F in TiF_4. We note that the $\sigma_{iso}\rightarrow\delta_{iso}$ and $\sigma_{csa}\rightarrow\delta_{csa}$ relationships derived here for terminal F species in TiF_4 provide suitable transformation functions for nonbridging Ti−F−□ fluorines that may be present in other titanium fluorides and oxyfluorides.

For all four GA-predicted structures, we obtain simulated ^{19}F spectra that are in close agreement with the experimental $TiOF_2$ spectrum (see Figure 11 for structure 4 and SI Figure S13 for all four GA-predicted structures), with average chemical shift values ranging from 22.6 to 25.4 ppm (SI Table S11). Moreover, the chemical shift anisotropies are well modeled, as evidenced by the correct reproduction of the spinning sidebands. The simulated and experimental spectra are not perfectly superimposed due to slightly different averages and larger spreads in the calculated chemical shift values compared to the experimental data. This discrepancy is not altogether unexpected, given the large chemical shift range of ^{19}F (over 1000 ppm[100]), the inherent uncertainty in our $\sigma_{iso}\rightarrow\delta_{iso}$ relationship, and the use of finite-size 4×4×4 structural models as approximations to the experimental structure.

Both the simulated PDF and ^{19}F NMR spectra show good agreement with the corresponding experimental data, with particularly good agreement in the case of the PDF data for

https://doi.org/10.1021/jacs.4c06304
J. Am. Chem. Soc. 2024, 146, 21889−21902

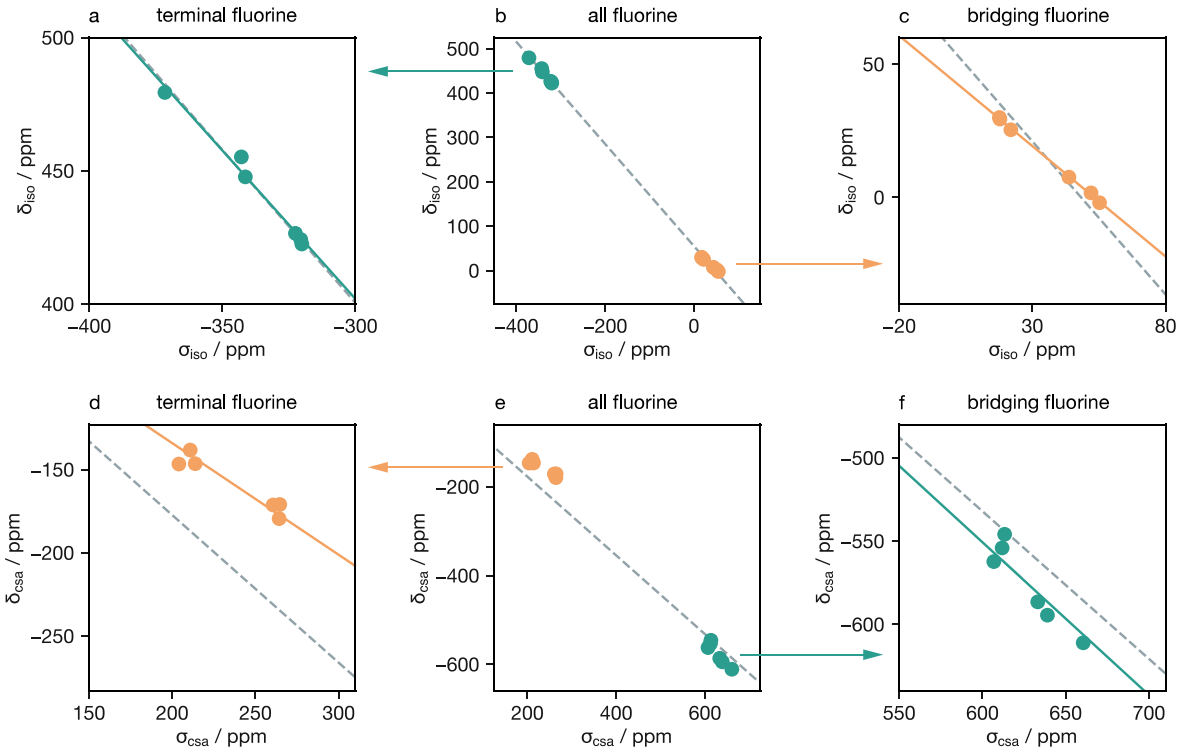

Figure 10. ^{19}F σ_{iso} and σ_{csa} values for TiF_4 from DFT calculations (VASP, PBE + DFT-D3), plotted against the corresponding experimental δ_{iso} and δ_{csa} values, respectively.[41] Panels (b) and (e) show all data and corresponding linear-least-squares fits (dashed lines). Panels (a) and (c), and (d) and (f), show the same data, selecting values for terminal F and bridging F only, respectively. Each panel shows the original linear model obtained from fitting to the full data set (dashed lines) and a revised linear model obtained by fitting to the corresponding data subset only (solid lines). The resulting best-fit linear models are $\delta_{iso} = -0.830\sigma_{iso} + 44.1$ and $\delta_{csa} = -0.671\sigma_{csa}$ for bridging F, and $\delta_{iso} = -1.116\sigma_{iso} + 67.2$ and $\delta_{csa} = -0.918\sigma_{csa}$ for terminal F.

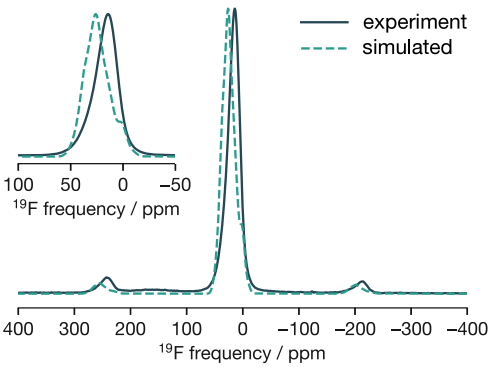

Figure 11. Experimental (solid line) and simulated (dashed line) ^{19}F MAS (64 kHz) NMR spectra of ReO_3-type $TiOF_2$ (GA-predicted structure 4).

GA-predicted structure 4. We therefore conclude that our DFT-derived cluster expansion model correctly describes the form of anion short-range order in ReO_3-type $TiOF_2$, and we consider structure 4, obtained from our GA structure prediction, as a representative structural model for the experimental samples considered in this work.

3.5. Lithium Intercalation and the Effect of O/F Order versus Disorder. ReO_3-type $TiOF_2$ has previously been considered as a potential lithium-ion electrode material.[30,31] Our results above indicate that ReO_3-type $TiOF_2$ exhibits a specific short-range anion ordering consisting of preferential *cis*-TiO_2F_4 titanium coordination, which gives rise to correlated disorder at longer length scales. Our analysis of the relative energies of different anion configurations shows that there are a large number of low-energy anion configurations that are expected to be competitive under synthesis conditions (Figure 4), indicating that the precise anion configuration in ReO_3-type $TiOF_2$ might depend on the choice of synthesis protocols, suggesting a possible route to modulating technologically relevant properties, such as lithium intercalation behavior.

Having predicted and validated structural models for "as-synthesized" ReO_3-type $TiOF_2$, we now consider the effect of variation in local anion structure on lithium intercalation properties. To this end, we computed the dilute limit intercalation voltage for all possible interstitial sites in three exemplar structures with varying degrees of anion ordering: these structures comprise a 4×4×4 supercell of the lowest energy 2×2×2 structure, which is fully ordered with all-*cis*-Ti[O_2F_4] coordination, the partially disordered GA-predicted structure 4, and a maximally disordered 4×4×4 special quasirandom structure (SQS), which approximates the O/F correlations for an infinite lattice with a fully random (maximum-entropy) distribution of anions.[101,102]

Figure 12 presents calculated lithium intercalation energies and estimated mean values for each exemplar structure. The fully ordered all-*cis*-Ti[O_2F_4] structure has only three non-equivalent interstitial sites and therefore has a relatively narrow distribution of lithium intercalation energies, with a mean of −1.53 eV. GA-predicted structure 4 is partially disordered, and all 64 cubic interstitial sites in the 4×4×4 supercell are therefore inequivalent by symmetry. This gives a broader spread in lithium intercalation energies of more than ∼1 eV, with an estimated mean of (−2.44 ± 0.05) eV. The SQS

https://doi.org/10.1021/jacs.4c06304
J. Am. Chem. Soc. 2024, 146, 21889−21902

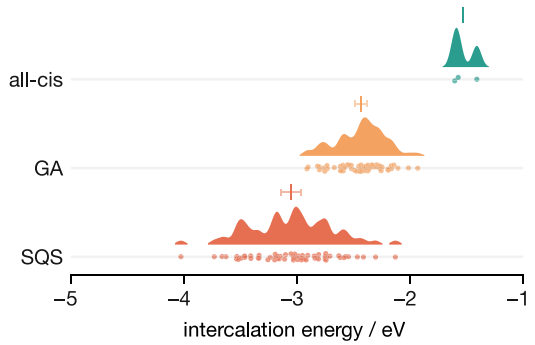

Figure 12. Effect of changing O/F substructure on lithium intercalation energies into cubic $TiOF_2$. Data are shown as raincloud plots[98] for three exemplar structures: (top) the fully ordered all-*cis*Ti[O_2F_4] structure; (middle) a 4×4×4 supercell genetic-algorithm-predicted structure (GA structure 4); and (bottom) the 4×4×4-supercell special quasirandom structure. For each data set, the points show individual calculated intercalation energies, and the solid distribution shows a kernel density estimate of the distribution of intercalation energies. Error bars show the 95% compatibility interval for the estimated mean of each data set, obtained by bootstrap resampling of the original data.[103]

structure is, again, more disordered than the GA-predicted structure and has an even broader spread in lithium intercalation energies (∼2 eV) and an estimated mean of (-3.06 ± 0.09) eV.

These results show that the lithium intercalation energy for ReO_3-type $TiOF_2$ is sensitive to the precise arrangement of oxygen and fluorine atoms within the host structure, with the mean intercalation energy shifting by >1.5 eV between the fully ordered all-*cis*Ti[O_2F_4] structure and the 4×4×4 special quasirandom structure considered here. In general, as the anion substructure becomes more configurationally disordered, the intercalation energy shifts to more negative values, while the distribution of lithium intercalation energies becomes broader. This result suggests that the electrochemical properties of ReO_3-type $TiOF_2$, and, by analogy, other heteroanionic intercalation electrode materials may be modulated through directed synthesis protocols that produce samples with different degrees of short-range anion order.

4. SUMMARY AND CONCLUSIONS

Heteroanionic materials offer a rich chemical space for developing new materials with targeted properties. To understand and control the properties of heteroanionic materials requires a detailed characterization of their structures—in particular, the specific arrangement of the component anions. Resolving the anionic substructure of anion-disordered oxyfluorides is particularly challenging because X-ray and neutron Bragg scattering experiments give only an average structural description. Resolving local structural details in anion-disordered oxyfluorides, therefore, requires using alternative complementary experimental or computational techniques.

Here, we have presented a study of the anionic substructure in the exemplar transition-metal oxyfluoride ReO_3-type $TiOF_2$, using a combination of X-ray PDF, ^{19}F NMR, DFT modeling, and genetic-algorithm structure prediction. We find that ReO_3-type $TiOF_2$ exhibits strong short-range ordering characterized by preferential *cis*-O_2F_4 coordination around titanium. This *cis*-coordination of titanium allows titanium cations to move away from the center of their coordination octahedra to give shorter Ti−O bonds (and longer Ti−F bonds), giving a net increase in total Ti−X bond strength, relative to more symmetric *trans*-O_2F_4 titanium coordination. This preferential *cis*-TiO_2F_4 coordination also gives rise to correlated anion disorder,[39] where the configuration of oxygen and fluorine ions decorrelates with separation, resulting in long-range anion disorder that is consistent with the average $Pm\bar{3}m$ structure model previously proposed from X-ray powder diffraction data.[34]

To obtain structural models that incorporate this correlated disorder, we used genetic algorithm structure prediction to generate partially disordered supercells. We then validated these structural models by generating simulated X-ray PDF and ^{19}F NMR data, which we compared to equivalent experimental data for our synthesized $TiOF_2$ sample. For the simulation of the ^{19}F NMR spectrum, we used new empirical linear transformation functions to convert from calculated shielding values, σ_{iso} and σ_{csa}, to predicted chemical shift values, δ_{iso} and δ_{csa}, which we derived by fitting calculated σ_{iso} and σ_{csa} values for bridging fluoride ions in TiF_4 to previously published experimental data.[41] We expect the resulting linear transformation functions to be generally applicable for calculating ^{19}F NMR spectra of other titanium oxyfluorides. For both the X-ray PDF and ^{19}F NMR data, our simulated data agree well with the corresponding experimental data, indicating that our genetic-algorithm-predicted structures reproduce well the short-range structure of our sample.

We then considered the effect of variations in anionic short-range order on the lithium intercalation properties of ReO_3-type $TiOF_2$. By performing additional DFT calculations, we showed that the local anion substructure can have a significant effect on lithium intercalation voltages, with an example fully ordered low-energy structure and the maximally disordered special quasirandom 4×4×4 supercell structure showing a difference of mean lithium intercalation voltage of >1.5 V as well as a large increase in the spread of intercalation voltage values. Because the precise short-range structure of ReO_3-type $TiOF_2$ may be affected by different synthesis protocols, this result indicates that it may be possible to tune the electrochemical intercalation behavior of $TiOF_2$—and, by analogy, of other transition-metal heteroanionic materials—through careful design of synthesis routes.

The work presented here demonstrates how the detailed local structure of heteroanionic oxyfluorides can be resolved using a combination of experimental and computational methods. By combining X-ray PDF analysis and ^{19}F NMR spectroscopy with DFT modeling and GA structure prediction, we have identified a revised structural model for ReO_3-type $TiOF_2$ that is consistent between our experimental and computational analyses. We have also identified how the details of local coordination geometry and bonding direct short-range order in this material, through anions adopting local configurations that maximize Ti−(O/F) bond strength. The general strategy presented here is expected to be generally applicable to other anion-disordered oxyfluorides, where similar short-range deviations from the average crystallographic structure obtained from conventional diffraction methods are also likely.

https://doi.org/10.1021/jacs.4c06304
J. Am. Chem. Soc. 2024, 146, 21889−21902

■ ASSOCIATED CONTENT

Data Availability Statement

Data and plotting scripts for Figures 2−4, 6−8, and 10−12 are available on GitHub.[104] This repository also includes CIF files for TiF_4 optimized using DFT (atomic positions only), using CASTEP, VASP without DFT-D3, and VASP with DFT-D3, and inputs and outputs for all DFT calculations used to train the cluster expansion (CE) model, for the CE model training, for the genetic- algorithm structure prediction calculations, and for DFT calculations of lithium intercalation into the GA-predicted 4×4×4 $TiOF_2$ supercell (model 4).

Supporting Information

The Supporting Information is available free of charge at https://pubs.acs.org/doi/10.1021/jacs.4c06304.

X-ray diffraction analysis for ReO_3-type $TiOF_2$; Pair Distribution Function data for $TiOF_4$ between 8 and 40 Å; additional details of the cluster expansion model fitting and model ECIs; details of the genetic-algorithm structure prediction scheme; structural analysis of the GA-predicted structures; correlation between calculated σ_{iso} and experimental δ_{iso} values for ^{19}F in titanium (oxy)fluorides; Haeberlen convention used to define the shielding and chemical shift NMR parameters; details about calculations using the NMR-CASTEP code; previously reported relationships between calculated σ_{iso} and experimental δ_{iso} values for ^{19}F in inorganic fluorides; derivation of an empirical linear relation between calculated σ_{iso} and experimental δ_{iso} values for ^{19}F in titanium (oxy)fluorides; effect of DFT calculation method on atomic positions for TiF_4; and simulated ^{19}F MAS NMR spectra for all four 4×4×4 GA-predicted structural models (PDF)

■ AUTHOR INFORMATION

Corresponding Authors

Christophe Legein − *Institut des Molécules et des Matériaux du Mans (IMMM), UMR 6283 CNRS, Le Mans Université, 72085 Le Mans Cedex 9, France;* orcid.org/0000-0001-7426-8817; Email: christophe.legein@univ-lemans.fr

Benjamin J. Morgan − *Department of Chemistry, University of Bath, Claverton Down BA2 7AY, United Kingdom; The Faraday Institution, Didcot OX11 0RA, United Kingdom;* orcid.org/0000-0002-3056-8233; Email: b.j.morgan@bath.ac.uk

Damien Dambournet − *Sorbonne Université, CNRS, Physico-chimie des électrolytes et nano-systèmes interfaciaux, PHENIX, F-75005 Paris, France; Réseau sur le Stockage Electrochimique de l'Energie (RS2E), 80039 Amiens Cedex, France;* orcid.org/0000-0003-3831-2643; Email: damien.dambournet@sorbonne-universite.fr

Authors

Alexander G. Squires − *School of Chemistry, University of Birmingham, Birmingham B15 2TT, United Kingdom; The Faraday Institution, Didcot OX11 0RA, United Kingdom;* orcid.org/0000-0001-6967-3690

Monique Body − *Institut des Molécules et des Matériaux du Mans (IMMM), UMR 6283 CNRS, Le Mans Université, 72085 Le Mans Cedex 9, France;* orcid.org/0000-0002-5895-3731

Wei Li − *Sorbonne Université, CNRS, Physico-chimie des électrolytes et nano-systèmes interfaciaux, PHENIX, F-75005 Paris, France; Réseau sur le Stockage Electrochimique de l'Energie (RS2E), 80039 Amiens Cedex, France*

Mario Burbano − *Sorbonne Université, CNRS, Physico-chimie des électrolytes et nano-systèmes interfaciaux, PHENIX, F-75005 Paris, France; Réseau sur le Stockage Electrochimique de l'Energie (RS2E), 80039 Amiens Cedex, France*

Mathieu Salanne − *Sorbonne Université, CNRS, Physico-chimie des électrolytes et nano-systèmes interfaciaux, PHENIX, F-75005 Paris, France; Réseau sur le Stockage Electrochimique de l'Energie (RS2E), 80039 Amiens Cedex, France;* orcid.org/0000-0002-1753-491X

Thibault Charpentier − *Université Paris-Saclay, CEA, CNRS, NIMBE, 91191 Gif-sur-Yvette Cedex, France;* orcid.org/0000-0002-3034-1389

Olaf J. Borkiewicz − *X-ray Science Division, Advanced Photon Source, Argonne National Laboratory, Argonne, Illinois 60439, United States*

Complete contact information is available at: https://pubs.acs.org/10.1021/jacs.4c06304

Notes

The authors declare no competing financial interest.

■ ACKNOWLEDGMENTS

The work done at the Advanced Photon Source, an Office of Science User Facility operated for the U.S. Department of Energy (DOE) Office of Science by Argonne National Laboratory, was supported by the U.S. DOE under Contract No. DE-AC02-06CH11357. C.L. and D.D. wish to thank the French fluorine network for continuous support. We thank Madhu Channabasappa for assistance in Rietveld analysis. B.J.M. acknowledges support from the Royal Society (Grant Nos. UF130329 and URF/R/191006). B.J.M. and A.G.S. acknowledge support from the Faraday Institution (FIRG016 and FIRG017). T.C. acknowledges support from the TGCC (VASP NMR calculations) with access to the HPC resources of under the allocation DARI-A0070906303 (2019) attributed by GENCI (Grand Equipement National de Calcul Intensif). We are grateful to the UK Materials and Molecular Modelling Hub for computational resources, which is partially funded by EPSRC (EP/P020194/1). This research made use of the Balena High Performance Computing (HPC) Service at the University of Bath. Part of the computations presented in this work has been carried out at the Centre Régional de Calcul Intensif des Pays de la Loire (CCIPL), financed by the French Research Ministry, the Région Pays de la Loire, and Nantes University. CCIPL is thanked for the CASTEP license financial support.

■ REFERENCES

(1) Harada, J. K.; Charles, N.; Poeppelmeier, K. R.; Rondinelli, J. M. Heteroanionic Materials by Design: Progress Toward Targeted Properties. *Adv. Mater.* **2019**, *31*, 1805295.

(2) Kageyama, H.; Hayashi, K.; Maeda, K.; Attfield, J. P.; Hiroi, Z.; Rondinelli, J. M.; Poeppelmeier, K. R. Expanding frontiers in materials chemistry and physics with multiple anions. *Nat. Commun.* **2018**, *9*, 772.

(3) Charles, N.; Saballos, R. J.; Rondinelli, J. M. Structural Diversity from Anion Order in Heteroanionic Materials. *Chem. Mater.* **2018**, *30*, 3528.

(4) Ghorpade, U. V.; Suryawanshi, M. P.; Green, M. A.; Wu, T.; Hao, X.; Ryan, K. M. Emerging Chalcohalide Materials for Energy Applications. *Chem. Rev.* **2023**, *123*, 327−378.

(5) Wagner, N.; Seshadri, R.; Rondinelli, J. M. Property control from polyhedral connectivity in ABO_3 oxides. *Phys. Rev. B* **2019**, *100*, 064101.
(6) Nicolson, A.; Breternitz, J.; Kavanagh, S. R.; Tomm, Y.; Morita, K.; Squires, A. G.; Tovar, M.; Walsh, A.; Schorr, S.; Scanlon, D. O. Interplay of Static and Dynamic Disorder in the Mixed-Metal Chalcohalide $Sn_2SbS_2I_3$. *J. Am. Chem. Soc.* **2023**, *145*, 12509−12517.
(7) Zhao, L. D.; Berardan, D.; Pei, Y. L.; Byl, C.; Pinsard-Gaudart, L.; Dragoe, N. $Bi_{1-x}Sr_xCuSeO$ oxyselenides as promising thermoelectric materials. *Appl. Phys. Lett.* **2010**, *97*, 092118.
(8) Zhang, K.; Liu, C.; Huang, F.; Zheng, C.; Wang, W. Study of the electronic structure and photocatalytic activity of the BiOCl photocatalyst. *Appl. Catal. B: Env.* **2006**, *68*, 125−129.
(9) Gou, G.; Zhao, M.; Shi, J.; Harada, J. K.; Rondinelli, J. M. Anion Ordered and Ferroelectric Ruddlesden-Popper Oxynitride $Ca_3Nb_2N_2O_5$ for Visible-Light-Active Photocatalysis. *Chem. Mater.* **2020**, *32*, 2815.
(10) Morgan, B. J. Mechanistic Origin of Superionic Lithium Diffusion in Anion-Disordered Li_6PS_5X Argyrodites. *Chem. Mater.* **2021**, *33*, 2004.
(11) McColl, K.; House, R. A.; Rees, G. J.; Squires, A. G.; Coles, S. W.; Bruce, P. G.; Morgan, B. J.; Islam, M. S. Transition metal migration and O_2 formation underpin voltage hysteresis in oxygen-redox disordered rocksalt cathodes. *Nature Commun.* **2022**, *13*, 5275.
(12) Coles, S. W.; Falkowski, V.; Geddes, H. S.; Pérez, G. E.; Booth, S. G.; Squires, A. G.; O'Rourke, C.; McColl, K.; Goodwin, A. L.; Cussen, S. A.; Clarke, S. J.; Islam, M. S.; Morgan, B. J. Anion-polarisation-directed short-range-order in antiperovskite Li_2FeSO. *J. Mater. Chem. A* **2023**, *11*, 13016.
(13) Squires, A. G.; Scanlon, D. O. Understanding the limits to short-range order suppression in many-component disordered rock salt lithium-ion cathode materials. *J. Mater. Chem. A* **2023**, *11*, 13765.
(14) Proffen, T.; Billinge, S. J. L.; Egami, T.; Louca, D. Structural analysis of complex materials using the atomic pair distribution function − a practical guide. *Z. Kristal. Cryst. Mater.* **2003**, *218*, 132.
(15) Du, L.-S.; Wang, F.; Grey, C. P. High-Resolution ^{19}F MAS and $^{19}F-^{113}Cd$ REDOR NMR Study of Oxygen/Fluorine Ordering in Oxyfluorides. *J. Sol. Stat. Chem.* **1998**, *140*, 285.
(16) Du, L.-S.; Samoson, A.; Tuherm, T.; Grey, C. P. $^{19}F/^{23}Na$ Double Resonance MAS NMR Study of Oxygen/Fluorine Ordering in the Oxyfluoride $Na_5W_3O_9F_5$. *Chem. Mater.* **2000**, *12*, 3611.
(17) Choy, J.-H.; Kim, J.-Y.; Kim, S.-J.; Sohn, J.-S.; Han, O. H. New Dion-Jacobson-Type Layered Perovskite Oxyfluorides, $ASrNb_2O_6F$ (A = Li, Na, and Rb). *Chem. Mater.* **2001**, *13*, 906.
(18) Du, L.-S.; Schurko, R. W.; Kim, N.; Grey, C. P. Solid-State ^{93}Nb, ^{19}F, and ^{113}Cd Nuclear Magnetic Resonance Study of Niobium Oxyfluorides: Characterization of Local Distortions and Oxygen/Fluorine Ordering. *J. Phys. Chem. A* **2002**, *106*, 7876.
(19) Köhler, J.; Simon, A.; van Wüllen, L.; Cordier, S.; Roisnel, T.; Poulain, M.; Somer, M. Structures and Properties of $NbOF_3$ and $TaOF_3$ − With a Remark to the O/F Ordering in the SnF_4 Type Structure. *Z. Anorg. Allg. Chem.* **2002**, *628*, 2683.
(20) Le Berre, F.; Crosnier-Lopez, M.-P.; Galven, C.; Fourquet, J.-L.; Legein, C.; Body, M.; Buzaré, J.-Y. Ca^{2+}/vacancies and O^{2-}/F^- ordering in new oxyfluoride pyrochlores $Li_{2x}Ca_{1.5-x}\square_{0.5-x}M_2O_6F$ (M = Nb, Ta) for $0 \leqslant x \leqslant 0.5$. *Dalton Trans.* **2007**, 2457.
(21) Alam, T. M.; Clawson, J. S.; Bonhomme, F.; Thoma, S. G.; Rodriguez, M. A.; Zheng, S.; Autschbach, J. A Solid-State NMR, X-ray Diffraction, and Ab Initio Investigation into the Structures of Novel Tantalum Oxyfluoride Clusters. *Chem. Mater.* **2008**, *20*, 2205.
(22) Sronek, L.; Lhoste, J.; Gaudon, M.; Legein, C.; Buzaré, J.-Y.; Body, M.; Crinière, G.; Tressaud, A.; Pechev, S.; Demourgues, A. Probing the Local Environments of Fluorine in Ce-Based Fluorite-Type Oxyfluorides with ^{19}F MAS NMR Spectroscopy. *J. Phys. Chem. C* **2008**, *112*, 860.
(23) Galven, C.; Legein, C.; Body, M.; Fourquet, J.-L.; Buzare, J.-Y.; Le Berre, F.; Crosnier-Lopez, M.-P. New Oxyfluoride Pyrochlores $Li_{2-x}La_{(1+x)/3}\square_{(2x-1)/3}B_2O_6F$ (B = Nb, Ta): Average and Local Structure Characterization by XRD, TEM and F Solid-State NMR Spectroscopy. *Eur. J. Inorg. Chem.* **2010**, *2010*, 5272.
(24) Griffin, J. M.; Yates, J. R.; Berry, A. J.; Wimperis, S.; Ashbrook, S. E. High-Resolution ^{19}F MAS NMR Spectroscopy: Structural Disorder and Unusual *J* Couplings in a Fluorinated Hydroxy-Silicate. *J. Am. Chem. Soc.* **2010**, *132*, 15651.
(25) Dabachi, J.; Body, M.; Dittmer, J.; Fayon, F.; Legein, C. Structural refinement of the RT LaOF phases by coupling powder X-Ray diffraction, ^{19}F and ^{139}La solid state NMR and DFT calculations of the NMR parameters. *Dalton Trans.* **2015**, *44*, 20675.
(26) Dabachi, J.; Body, M.; Galven, C.; Boucher, F.; Legein, C. Preparation-Dependent Composition and O/F Ordering in NbO_2F and TaO_2F. *Inorg. Chem.* **2017**, *56*, 5219.
(27) Ding, F.; Griffith, K. J.; Koçer, C. P.; Saballos, R. J.; Wang, Y.; Zhang, C.; Nisbet, M. L.; Morris, A. J.; Rondinelli, J. M.; Poeppelmeier, K. R. Multimodal Structure Solution with ^{19}F NMR Crystallography of Spin Singlet Molybdenum Oxyfluorides. *J. Am. Chem. Soc.* **2020**, *142*, 12288.
(28) Pilania, G.; Ghosh, A.; Hartman, S. T.; Mishra, R.; Stanek, C. R.; Uberuaga, B. P. Anion order in oxysulfide perovskites: Origins and implications. *npj Comput. Mater.* **2020**, *6*, 71.
(29) Young, S. D.; Chen, J.; Sun, W.; Goldsmith, B. R.; Pilania, G. Thermodynamic Stability and Anion Ordering of Perovskite Oxynitrides. *Chem. Mater.* **2023**, *35*, 5975.
(30) Reddy, M. V.; Madhavi, S.; Subba Rao, G. V.; Chowdari, B. V. R. Metal oxyfluorides $TiOF_2$ and NbO_2F as anodes for Li-ion batteries. *J. Power Sour.* **2006**, *162*, 1312.
(31) Louvain, N.; Karkar, Z.; El-Ghozzi, M.; Bonnet, P.; Guérin, K.; Willmann, P. Fluorination of anatase TiO_2 towards titanium oxyfluoride $TiOF_2$: a novel synthesis approach and proof of the Li-insertion mechanism. *J. Mater. Chem. A* **2014**, *2*, 15308.
(32) Wang, J.; Cao, F.; Bian, Z.; Leung, M. K. H.; Li, H. Ultrafine single-crystal $TiOF_2$ nanocubes with mesoporous structure, high activity and durability in visible light driven photocatalysis. *Nanoscale* **2014**, *6*, 897.
(33) Hou, C.; Liu, H.; Li, Y. The preparation of three-dimensional flower-like $TiO_2/TiOF_2$ photocatalyst and its efficient degradation of tetracycline hydrochloride. *RSC Adv.* **2021**, *11*, 14957.
(34) Vorres, K.; Donohue, J. The structure of titanium oxydifluoride. *Acta Crystallogr.* **1955**, *8*, 25.
(35) Withers, R. L.; Brink, F.; Liu, Y.; Norén, L. Cluster chemistry in the solid state: Structured diffuse scattering, oxide/fluoride ordering and polar behaviour in transition metal oxyfluorides. *Polyhedron* **2007**, *26*, 290.
(36) Brink, F. J.; Withers, R. L.; Norén, L. An Electron Diffraction and Crystal Chemical Investigation of Oxygen/Fluorine Ordering in Niobium Oxyfluoride, NbO_2F. *J. Sol. Stat. Chem.* **2002**, *166*, 73.
(37) Pérez-Flores, J. C.; Villamor, R.; Ávila-Brande, D.; Amores, J. M. G.; Morán, E.; Kuhn, A.; García-Alvarado, F. VO_2F: A new transition metal oxyfluoride with high specific capacity for Li ion batteries. *J. Mater. Chem. A* **2015**, *3*, 20508.
(38) Morelock, C. R.; Greve, B. K.; Cetinkol, M.; Chapman, K. W.; Chupas, P. J.; Wilkinson, A. P. Role of Anion Site Disorder in the Near Zero Thermal Expansion of Tantalum Oxyfluoride. *Chem. Mater.* **2013**, *25*, 1900.
(39) Keen, D. A.; Goodwin, A. L. The crystallography of correlated disorder. *Nature* **2015**, *521*, 303.
(40) Overy, A. R.; Cairns, A. B.; Cliffe, M. J.; Simonov, A.; Tucker, M. G.; Goodwin, A. L. Design of crystal-like aperiodic solids with selective disorder−phonon coupling. *Nature Commun.* **2016**, *7*, 10445.
(41) Murakami, M.; Noda, Y.; Takegoshi, K. Terminal and bridging fluorine ligands in TiF_4 as studied by ^{19}F NMR in solids. *Sol. Stat. Nucl. Mag. Res.* **2019**, *101*, 82.
(42) Li, W.; Body, M.; Legein, C.; Dambournet, D. Identify OH groups in $TiOF_2$ and their impact on the lithium intercalation properties. *J. Sol. Stat. Chem.* **2017**, *246*, 113.

https://doi.org/10.1021/jacs.4c06304
J. Am. Chem. Soc. 2024, 146, 21889−21902

(43) Chupas, P. J.; Qiu, X.; Hanson, J. C.; Lee, P. L.; Grey, C. P.; Billinge, S. J. L. Rapid-acquisition pair distribution function (RA-PDF) analysis. *J. Appl. Crystallogr.* **2003**, *36*, 1342.
(44) Chupas, P. J.; Chapman, K. W.; Lee, P. L. Applications of an amorphous silicon-based area detector for high-resolution, high-sensitivity and fast time-resolved pair distribution function measurements. *J. Appl. Crystallogr.* **2007**, *40*, 463.
(45) Hammersley, A. P.; Svensson, S. O.; Hanfland, M.; Fitch, A. N.; Hausermann, D. Two-dimensional detector software: From real detector to idealised image or two-theta scan. *High Pres. Res.* **1996**, *14*, 235.
(46) Qiu, X.; Thompson, J. W.; Billinge, S. J. L. PDFgetX2: a GUI-driven program to obtain the pair distribution function from X-ray powder diffraction data. *J. Appl. Crystallogr.* **2004**, *37*, 678.
(47) Farrow, C. L.; Juhas, P.; Liu, J. W.; Bryndin, D.; Božin, E. S.; Bloch, J.; Proffen, T.; Billinge, S. J. L. PDFfit2 and PDFgui: Computer programs for studying nanostructure in crystals. *J. Phys.: Condens. Matter* **2007**, *19*, 335219.
(48) Egami, T.; Billinge, S. *Underneath the Bragg Peaks: Structural Analysis of Complex Materials*; Elsevier, 2012.
(49) Massiot, D.; Fayon, F.; Capron, M.; King, I.; Le Calve, S.; Alonso, B.; Durand, J.-O.; Bujoli, B.; Gan, Z.; Hoatson, G. Modelling one- and two-dimensional solid-state NMR spectra. *Magn. Reson. Chem.* **2002**, *40*, 70.
(50) Morgan, B. J. bsym: A basic symmetry module. *J. Open Source Soft.* **2017**, *2*, 370.
(51) Kresse, G.; Furthmüller, J. Efficient iterative schemes for ab initio total-energy calculations using a plane-wave basis set. *Phys. Rev. B* **1996**, *54*, 11169.
(52) Kresse, G.; Furthmüller, J. Efficiency of ab-initio total energy calculations for metals and semiconductors using a plane-wave basis set. *Comput. Mater. Sci.* **1996**, *6*, 15.
(53) Blöchl, P. E. Projector augmented-wave method. *Phys. Rev. B* **1994**, *50*, 17953.
(54) Perdew, J. P.; Ruzsinszky, A.; Csonka, G. I.; Vydrov, O. A.; Scuseria, G. E.; Constantin, L. A.; Zhou, X.; Burke, K. Restoring the Density-Gradient Expansion for Exchange in Solids and Surfaces. *Phys. Rev. Lett.* **2008**, *100*, 136406.
(55) Dudarev, S. L.; Liechtenstein, A. I.; Castell, M. R.; Briggs, G. A. D.; Sutton, A. P. Surface states on NiO (100) and the origin of the contrast reversal in atomically resolved scanning tunneling microscope images. *Phys. Rev. B* **1997**, *56*, 4900.
(56) Dudarev, S. L.; Botton, G. A.; Savrasov, S. Y.; Humphreys, C. J.; Sutton, A. P. Electron-energy-loss spectra and the structural stability of nickel oxide: An LSDA+U study. *Phys. Rev. B* **1998**, *57*, 1505.
(57) Morgan, B. J.; Watson, G. W. A DFT+U description of oxygen vacancies at the TiO_2 rutile (110) surface. *Surf. Sci.* **2007**, *601*, 5034.
(58) Morgan, B. J.; Watson, G. W. Intrinsic n-type Defect Formation in TiO_2: A Comparison of Rutile and Anatase from GGA+*U* Calculations. *J. Phys. Chem. C* **2010**, *114*, 2321.
(59) Morgan, B. J.; Watson, G. W. GGA+*U* description of lithium intercalation into anatase TiO_2. *Phys. Rev. B* **2010**, *82*, 144119.
(60) Morgan, B. J.; Watson, G. W. Role of Lithium Ordering in the Li_xTiO_2 Anatase→Titanate Phase Transition. *J. Phys. Chem. Lett.* **2011**, *2*, 1657.
(61) Morgan, B. J.; Madden, P. A. Lithium intercalation into TiO_2(B): A comparison of LDA, GGA, and GGA+U density functional calculations. *Phys. Rev. B* **2012**, *86*, 035147.
(62) Koketsu, T.; Ma, J.; Morgan, B. J.; Body, M.; Legein, C.; Dachraoui, W.; Giannini, M.; Demortière, A.; Salanne, M.; Dardoize, F.; Groult, H.; Borkiewicz, O. J.; Chapman, K. W.; Strasser, P.; Dambournet, D. Reversible magnesium and aluminium ions insertion in cation-deficient anatase TiO_2. *Nat. Mater.* **2017**, *16*, 1142.
(63) Ma, J.; Li, W.; Morgan, B. J.; Światowska, J.; Baddour-Hadjean, R.; Body, M.; Legein, C.; Borkiewicz, O. J.; Leclerc, S.; Groult, H.; Lantelme, F.; Laberty-Robert, C.; Dambournet, D. Lithium Intercalation in Anatase Titanium Vacancies and the Role of Local Anionic Environment. *Chem. Mater.* **2018**, *30*, 3078.
(64) Legein, C.; Morgan, B. J.; Fayon, F.; Koketsu, T.; Ma, J.; Body, M.; Sarou-Kanian, V.; Wei, X.-K.; Heggen, M.; Borkiewicz, O. J.; Strasser, P.; Dambournet, D. Atomic Insights into Aluminium-Ion Insertion in Defective Anatase for Batteries. *Angew. Chem., Int. Ed.* **2020**, *59*, 19247.
(65) van de Walle, A.; Asta, M.; Ceder, G. The alloy theoretic automated toolkit: A user guide. *Calphad* **2002**, *26*, 539.
(66) van de Walle, A. Multicomponent multisublattice alloys, nonconfigurational entropy and other additions to the Alloy Theoretic Automated Toolkit. *Calphad* **2009**, *33*, 266.
(67) Walle, A.; Ceder, G. Automating first-principles phase diagram calculations. *J. Phase Equilib.* **2002**, *23*, 348.
(68) Deringer, V. L.; Tchougréeff, A. L.; Dronskowski, R. Crystal Orbital Hamilton Population (COHP) Analysis As Projected from Plane-Wave Basis Sets. *J. Phys. Chem. A* **2011**, *115*, 5461.
(69) Maintz, S.; Deringer, V. L.; Tchougréeff, A. L.; Dronskowski, R. Analytic projection from plane-wave and PAW wavefunctions and application to chemical-bonding analysis in solids. *J. Comput. Chem.* **2013**, *34*, 2557.
(70) Maintz, S.; Deringer, V. L.; Tchougréeff, A. L.; Dronskowski, R. LOBSTER: A tool to extract chemical bonding from plane-wave based DFT. *J. Comput. Chem.* **2016**, *37*, 1030.
(71) Kuhne, T. D.; Iannuzzi, M.; Del Ben, M.; Rybkin, V. V.; Seewald, P.; Stein, F.; Laino, T.; Khaliullin, R. Z.; Schutt, O.; Schiffmann, F.; Golze, D.; Wilhelm, J.; Chulkov, S.; Bani-Hashemian, M. H.; Weber, V.; Borstnik, U.; Taillefumier, M.; Jakobovits, A. S.; Lazzaro, A.; Pabst, H.; Muller, T.; Schade, R.; Guidon, M.; Andermatt, S.; Holmberg, N.; Schenter, G. K.; Hehn, A.; Bussy, A.; Belleflamme, F.; Tabacchi, G.; Gloß, A.; Lass, M.; Bethune, I.; Mundy, C. J.; Plessl, C.; Watkins, M.; VandeVondele, J.; Krack, M.; Hutter, J. CP2K: An electronic structure and molecular dynamics software package - Quickstep: Efficient and accurate electronic structure calculations. *J. Chem. Phys.* **2020**, *152*, 194103.
(72) Perdew, J. P.; Burke, K.; Ernzerhof, M. Generalized Gradient Approximation Made Simple. *Phys. Rev. Lett.* **1996**, *77*, 3865.
(73) Grimme, S.; Antony, J.; Ehrlich, S.; Krieg, H. A consistent and accurate *ab initio* parametrization of density functional dispersion correction (DFT-D) for the 94 elements H-Pu. *J. Chem. Phys.* **2010**, *132*, 154104.
(74) Biswal, M.; Body, M.; Legein, C.; Sadoc, A.; Boucher, F. NbF_5 and TaF_5: Assignment of ^{19}F NMR resonances and chemical bond analysis from GIPAW calculations. *J. Sol. Stat. Chem.* **2013**, *207*, 208−217.
(75) Goedecker, S.; Teter, M.; Hutter, J. Separable dual-space Gaussian pseudopotentials. *Phys. Rev. B* **1996**, *54*, 1703−1710.
(76) Pickard, C. J.; Mauri, F. All-electron magnetic response with pseudopotentials: NMR chemical shifts. *Phys. Rev. B* **2001**, *63*, 245101.
(77) Yates, J. R.; Pickard, C. J.; Mauri, F. Calculation of NMR chemical shifts for extended systems using ultrasoft pseudopotentials. *Phys. Rev. B* **2007**, *76*, 024401.
(78) Kresse, G.; Joubert, D. From ultrasoft pseudopotentials to the projector augmented-wave method. *Phys. Rev. B* **1999**, *59*, 1758.
(79) Pedone, A.; Charpentier, T.; Menziani, M. C. Multinuclear NMR of $CaSiO_3$ Glass: Simulation from First-Principles. *Phys. Chem. Chem. Phys.* **2010**, *12*, 6054.
(80) We provide details about the Haeberlen convention,[105] used to define the shielding and chemical shift NMR parameters, in the SI.
(81) Bialowons, H.; Müller, M.; Müller, B. G. Titantetrafluorid−Eine überraschend einfache Kolumnarstruktur. *Z. Anorg. Allg. Chem.* **1995**, *621*, 1227.
(82) Segall, M. D.; Lindan, P. J. D.; Probert, M. J.; Pickard, C. J.; Hasnip, P. J.; Clark, S. J.; Payne, M. C. First-principles simulation: ideas, illustrations and the CASTEP code. *J. Phys.: Condens. Matter* **2002**, *14*, 2717.
(83) Clark, S. J.; Segall, M. D.; Pickard, C. J.; Hasnip, P. J.; Probert, M. I. J.; Refson, K.; Payne, M. C. First principles methods using CASTEP. *Z. Krist.−Cryst. Mater.* **2005**, *220*, 567.

https://doi.org/10.1021/jacs.4c06304
J. Am. Chem. Soc. 2024, 146, 21889−21902

(84) Li, W.; Corradini, D.; Body, M.; Legein, C.; Salanne, M.; Ma, J.; Chapman, K. W.; Chupas, P. J.; Rollet, A.-L.; Julien, C.; Zhagib, K.; Duttine, M.; Demourgues, A.; Groult, H.; Dambournet, D. High Substitution Rate in TiO_2 Anatase Nanoparticles with Cationic Vacancies for Fast Lithium Storage. *Chem. Mater.* **2015**, *27*, 5014.
(85) The relative intensities of ^{19}F NMR resonances in hydroxyfluorinated anatase TiO_2 can be assigned to distinct Ti_3−F, $Ti_2\square$−F, and $Ti\square_2$−F environments. The relative intensities of these NMR resonances are consistent with a preferential clustering of fluoride ions around titanium vacancies,[62,84] with this structural model supported by DFT calculations.[63,84,106] This clustering of fluoride ions around titanium vacancies is consistent with the expectation that Ti−O bonds are stronger than Ti−F bonds, which, in turn, is consistent with the iCOHP data we present in the main text. We, therefore, expect similar clustering of fluoride-ions around Ti vacancies to occur in ReO_3-type $TiOF_2$, causing Ti vacancies to have an average fluoride-ion coordination number greater than the average of four for the usual TiO_2F_4 coordination octahedra. Hence, we expect our estimated proportion of "non-bridging" F^- of 2.2% to correspond to a proportion of Ti vacancies of $\lesssim$0.5%.
(86) Pauling, L. The Principles Determining the Structure of Complex Ionic Crystals. *J. Am. Chem. Soc.* **1929**, *51*, 1010.
(87) Wolff, H.; Dronskowski, R. First-principles and molecular-dynamics study of structure and bonding in perovskite-type oxynitrides ABO_2N (A = Ca, Sr, Ba;B = Ta, Nb). *J. Comput. Chem.* **2008**, *29*, 2260.
(88) Yang, M.; Oró-Solé, J.; Rodgers, J. A.; Jorge, A. B.; Fuertes, A.; Attfield, J. P. Anion order in perovskite oxynitrides. *Nat. Chem.* **2011**, *3*, 47.
(89) Kim, Y.-I.; Woodward, P. M.; Baba-Kishi, K. Z.; Tai, C. W. Characterization of the Structural, Optical, and Dielectric Properties of Oxynitride Perovskites AMO_2N (A = Ba, Sr, Ca; M = Ta, Nb). *Chem. Mater.* **2004**, *16*, 1267.
(90) Attfield, J. P. Principles and Applications of Anion Order in Solid Oxynitrides. *Crys. Grow. Des.* **2013**, *13*, 4623.
(91) Porter, S. H.; Huang, Z.; Cheng, Z.; Avdeev, M.; Chen, Z.; Dou, S.; Woodward, P. M. Structural and magnetic properties of $RTiNO_2$ (R = Ce, Pr, Nd) perovskite nitride oxides. *J. Sol. Stat. Chem.* **2015**, *226*, 279.
(92) Pinlac, R. A. F.; Stern, C. L.; Poeppelmeier, K. R. New Layered Oxide-Fluoride Perovskites: $KNaNbOF_5$ and $KNaMO_2F_4$ (M = Mo^{6+}, W^{6+}). *Crystals* **2011**, *1*, 3−14.
(93) Jo, H.; Lee, M. H.; Ok, K. M. Order and Disorder: Toward the Thermodynamically Stable α-$BaMoO_2F_4$ from the Metastable Polymorph. *Chem. Mater.* **2021**, *33*, 1875−1882.
(94) Yan, M.; Tang, R.-L.; Liu, W.; Guo, S.-P. From $Ba_3Nb_2O_2F_{12}(H_2O)_2$ to $Ba_{0.5}NbO_2F_2(H_2O)$: Achieving Balanced Nonlinear Optical Performance by O/F Ratio Regulation. *Inorg. Chem.* **2022**, *61*, 20709−20715.
(95) Zakary, O.; Body, M.; Charpentier, T.; Sarou-Kanian, V.; Legein, C. Structural Modeling of O/F Correlated Disorder in $TaOF_3$ and $NbOF_{3-x}(OH)_x$ by Coupling Solid-State NMR and DFT Calculations. *Inorg. Chem.* **2023**, *62*, 16627−16640.
(96) Frevel, L. K.; Rinn, H. W. The crystal structure of NbO_2F and TaO_2F. *Acta Crystallogr.* **1956**, *9*, 626−627.
(97) The uncorrelated [F−O−O−F] model of Brink et al. has also been shown to give an improved fit to experimental PDF data for ReO_3-structured $TaOF_2$ versus a fully random $Pm\bar{3}m$ model.[36]
(98) Allen, M.; Poggiali, D.; Whitaker, K.; Marshall, T. R.; van Langen, J.; Kievit, R. A. Raincloud plots: a multi-platform tool for robust data visualization. *Well. Open Res.* **2019**, *4*, 63.
(99) In addition to the TiF_4 ^{19}F NMR DFT data calculated using VASP with the DFT-D3 correction that we discuss in the main text, we have also performed calculations using VASP and CASTEP, both without DFT-D3, with the latter included to reproduce the calculations of Murakami et al.[41] Further details and results for these additional TiF_4 ^{19}F NMR calculations are given in the SI.
(100) Harris, R. K.; Jackson, P. High-Resolution Fluorine-19 Magnetic Resonance of Solids. *Chem. Rev.* **1991**, *91*, 1427.
(101) Zunger, A.; Wei, S.-H.; Ferreira, L. G.; Bernard, J. E. Special quasirandom structures. *Phys. Rev. Lett.* **1990**, *65*, 353.
(102) Wei, S.-H.; Ferreira, L. G.; Bernard, J. E.; Zunger, A. Electronic properties of random alloys: Special quasirandom structures. *Phys. Rev. B* **1990**, *42*, 9622.
(103) Efron, B. Bootstrap Methods: Another Look at the Jackknife. *Ann. Stat.* **1979**, *7*, 1−26.
(104) Morgan, B. J. Data analysis for "Correlated Anion-Disorder in Heteroanionic Cubic $TiOF_2$, 2024. https://github.com/bjmorgan/data_TiOF2.
(105) Haeberlen, U. *Advances in magnetic resonance, in High Resolution NMR in Solids Selective Averaging*; Academic Press, 1976.
(106) Corradini, D.; Dambournet, D.; Salanne, M. Tuning the Electronic Structure of Anatase Through Fluorination. *Sci. Rep.* **2015**, *5*, 11553.

https://doi.org/10.1021/jacs.4c06304
J. Am. Chem. Soc. 2024, 146, 21889−21902